Cavity quantum electrodynamics with quantum dots in microcavities

Gudat, J.

Chapter 1

Introduction

Coherent optical manipulation of a single quantum dot (QD) is interesting for fundamental research and quantum information applications. This thesis focuses on enhancing the interaction of QDs with light by embedding the QDs in microcavities. This field of research is closely related to atomic physics, quantum optics, condensed matter physics, material science, and quantum information science. Atomic physics describes transitions between electronic energy levels via interaction with light. Quantum optics explains quantum mechanical properties of light and its dependence on optical resonators. Condensed matter physics and material science describe the self-assembly and properties of semiconductor QDs and semiconductor microcavity structures. Finally, quantum information science provides the main motivation for the research by describing quantum logic schemes that could be implemented with QDs embedded in microcavities. The overarching field of research is called *Quantum electrodynamics* (QED) and when dealing with microcavities in particular *cavity QED*.

The speed at which the semiconductor industry is establishing new generations of computers is determined by the technological progress in reducing the physical size of an elementary bit and the elementary gate operations. The smaller the size, the shorter the connections, and the lower the energy consumption (and associated heat dissipation) per gate operation. Eventually the elementary building blocks will become so small that quantum effects, such as quantum superpositions of bit values (referred to as *quantum bits* or *qubits*) and quantum entanglement between such quantum bits will become important for the functionality of the computation. Of course quantum mechanics is already essential for understanding the operation of semiconductor based 'classical' computation but here we are concerned with quantum properties of the logic operations leading to the concept of quantum computation.

Currently there are several experimental routes towards quantum computation, for example exploring trapped atoms and ions, superconducting circuits, quantum optics, and confined electron spins. The quantum bit of relevance to this thesis is an electron spin confined to a semiconductor QD. The QD itself is confined within a microcavity structure in order to efficiently interface with light.
Building a quantum computer is a world wide effort that started about 15 years ago and most likely will take many more years to build quantum systems that might outperform classical computers for certain tasks. Therefore it should be clear that in this thesis only one aspect of one particular scheme towards quantum computation will be addressed. This aspect is expressed by the title of this thesis: Cavity quantum electrodynamics with quantum dots in microcavities.

The long-term vision of controlling electron spins via single photons in microcavities will be presented in Sect. 1.1. Section 1.2 provides a list of scientific and technological challenges that have to be addressed. Several of these challenges are being addressed in parallel in various forms of collaborations, in particular with researchers at the University of California Santa Barbara. This thesis focuses on several of those challenges, in particular the optical properties of oxide-aperture micropillar cavities, the control of their birefringence by strain, the properties of photonic crystals that are actively positioned around QDs, the theoretical study of electron spins jumps in QDs, and the study of quantum information protocols. Section 1.3 describes the growth and properties of single QDs. They allow a total quantization in all three spatial dimensions leading to discrete electron energy levels. Implementation of single QD structures has been an active field of research since their first demonstrations in the mid 90ies [1–3]. Coherent manipulation of single QDs is a promising path for realizing quantum computing. Section 1.4 describes the optical microcavities used in the experiments presented in this thesis. Section 1.5 describes the theory of cavity quantum electrodynamics.

Chapter 2 presents the experimental measurement techniques that have been developed. Chapter 3 describes the optical mode profile in oxide-apertured micropillars. It is crucial to achieve an efficient coupling of photons to the cavity in order to achieve a high fidelity of the quantum bit operations. This is an important criterion allowing to connect these operations to eventually build a quantum computer. For successful implementation of quantum information processing with QDs in microcavities we need to have the fundamental mode

in our microcavities to be polarization degenerate. Furthermore, the QD transition frequency and the polarization-degenerate fundamental mode frequency have to be on resonance. Chapter 4 demonstrates how to systematically and permanently tune the cavities and the QD to fulfill these requirements. Growing self-assembled QDs is an art in itself. For our applications wavelength and position have to match the cavity properties. The self-assembled QDs are randomly growing on the surface of a non-matching lattice substrate. We developed a technique allowing to position QDs at the center of microcavities. The technique was successfully utilized to demonstrate measurements in the strong coupling regime with a QD in a photonic crystal (PC) cavity. Here, the accuracy for positioning a single QD is in the order of 10nm. Chapter 5 explains the positioning technique. Chapter 6 elaborates theoretically on how electron spin quantum jumps could be measured in a singly charged QD. This is one of the initial ideas that evolved when thinking about the use of single QDs in micropillar cavities. The following Chap. 7 presents a larger picture of how to use these devices for implementation of quantum computing in the weak-coupling cavity QED regime. Finally, by combining several techniques developed in previous chapters, Chap. 8 presents reflection spectroscopy measurements of QDs in micropillar cavities, those results utilize all the techniques developed in this thesis.

The nature of this complex solid-state research implies that many results have been obtained in close collaboration with several colleagues. Therefore it is appropriate to point out the support for the various chapters. My colleague Cristian Bonato contributed substantially in theoretical questions and practical matters to chapters 3, 4 and 8. For the same chapters samples were fabricated by Hyochul Kim in Santa Barbara. Theoretical input and ideas for Chaps. 3 and 4 were also provided by Martin van Exter. The work on active positioning QDs described in Chap. 5 is based on work I carried out in Santa Barbara. For the same chapter, photonic crystal samples were provided by Susanna Thon and measured in Leiden. Chapter 6 is strongly based on theoretical work by Martin van Exter and earlier work by Gerard Nienhuis. Chapter 7 is based on joint theoretical work of Cristian Bonato and Sumant Oemrawsingh. Contributions by others not mentioned here are co-authors of the published papers referred to in each chapter.

1.1 Controlling electron spin interactions via photons

In recent years many groundbreaking results have been reported which indicate that optical and electrical control of single electron spins within optical nano and micro resonators is a promising approach to classical and quantum data processing. For example, strong coupling between single semiconductor QDs and optical modes in photonic crystals [4] and microcavities [5] has been observed, electron spin storage has been demonstrated with ms storage times [6, 7], and phase coherence times of spins between 10ns and 100ns have been observed by using applied magnetic fields [8]. Furthermore optical pumping [9], spin echo techniques, charging of one electron at the time in nanostructures [10], formation of double-dot 'molecules' [11–13], exciton Rabi oscillations in single QDs [14], and semiconductor single-photon [15, 16] and entangled-photon sources [17, 18] have been demonstrated.

The main reason for being optimistic about electron spin quantum computing is that the electron spin, playing the role of a qubit in the schemes described below, is manipulated and read out by fast spin-dependent optical processes that couple efficiently to external modes. Compared to schemes based on trapped ions /atoms this system has the advantage that the QDs, playing a similar role as the trapped ions/atoms, are directly grown at the center of optical cavities what allows for excellent optical coupling and what removes the complexity of trapping particles during the final experiments. The price to pay for this is that the qubit, in the form of a QD confined electron (or in some schemes a hole) spin, is quite strongly interacting with its solid-state environment. In the end, the relevant parameter is the qubit coherence time over the single and two-qubit gate times. In solid-state systems the electron/-hole spin decoherence time (typically in the nano- to microsecond range for solid-state systems [19]) over the optical readout/control gate (reported to be as short as 300ps in cavity enhanced configurations) can exceed 10.000.

A major complication for this solid-state based approach is that the required material growth and clean room fabrication techniques are very specialized, expensive, and time consuming. As a result a significant research team and infrastructure is required in order to make progress.

1.1.1 Vision

It will be demanding to write and read single electron spins confined in QDs, but it will be even more challenging to have controlled interactions between specific spins. Such interactions will be crucial for quantum gate operations. Recently an ingenious scheme has been proposed that uses photonic qubits to implement interactions between stationary qubits, here the electron spins, through quantum teleportation. The general idea has been put forward in a series of theoretical papers [20–23], starting with the invention of cluster state quantum computation. To implement cluster-state quantum computation an array (2 or higher dimensional) of basis qubits (here the electron spins) has to be prepared in a cluster-state through nearest neighbor two-qubit gate operations. For example, the most elementary cluster state of two qubits is a two-particle (entangled) Bell state. After the cluster state has been established, which basically produces an entangled state involving all the qubits, specific measurements on individual qubits will 'program' the quantum computer. After this step a specific input state can be provided and the cluster state quantum computation will be performed. The special feature of this approach is that all the quantum correlations are introduced in the system before any specific calculation or input is considered. Only local (single qubit) operations and measurements are needed afterwards. Therefore the main challenge is to produce a cluster state. To produce this cluster state for individual electron spins (each in a single QD), a hybrid, solid-state/photonics, approach has been put forward. The hybrid approach combines advantages of different systems, quantum information is stored in a one qubit type and processed in another one. Figure 1.1 illustrates how two electron spins can undergo a two-qubit gate operation (that can result in an entangled state and therefore can be used for cluster state quantum computation).

The two-qubit gates can be implemented via the following steps:

1. Two independent electron spin qubits will first be prepared in two separated QD micropillar structures. Hence, we have two prepared spin states:

$$|\Psi\rangle_{Spin1} = \alpha_1 |\uparrow\rangle_1 + \beta_1 |\downarrow\rangle_1 , \tag{1.1}$$

$$|\Psi\rangle_{Spin2} = \alpha_2 |\uparrow\rangle_2 + \beta_2 |\downarrow\rangle_2 . \tag{1.2}$$

Together they form the following product state

$$|\Psi\rangle_{Spin1,Spin2} = |\Psi\rangle_{Spin1} \otimes |\Psi\rangle_{Spin2} = \alpha |\uparrow\uparrow\rangle + \beta |\uparrow\downarrow\rangle + \gamma |\downarrow\uparrow\rangle + \delta |\downarrow\downarrow\rangle , \tag{1.3}$$

with $\alpha = \alpha_1\alpha_2$, $\beta = \alpha_1\beta_2$, $\gamma = \beta_1\alpha_2$ and $\delta = \beta_1\beta_2$.

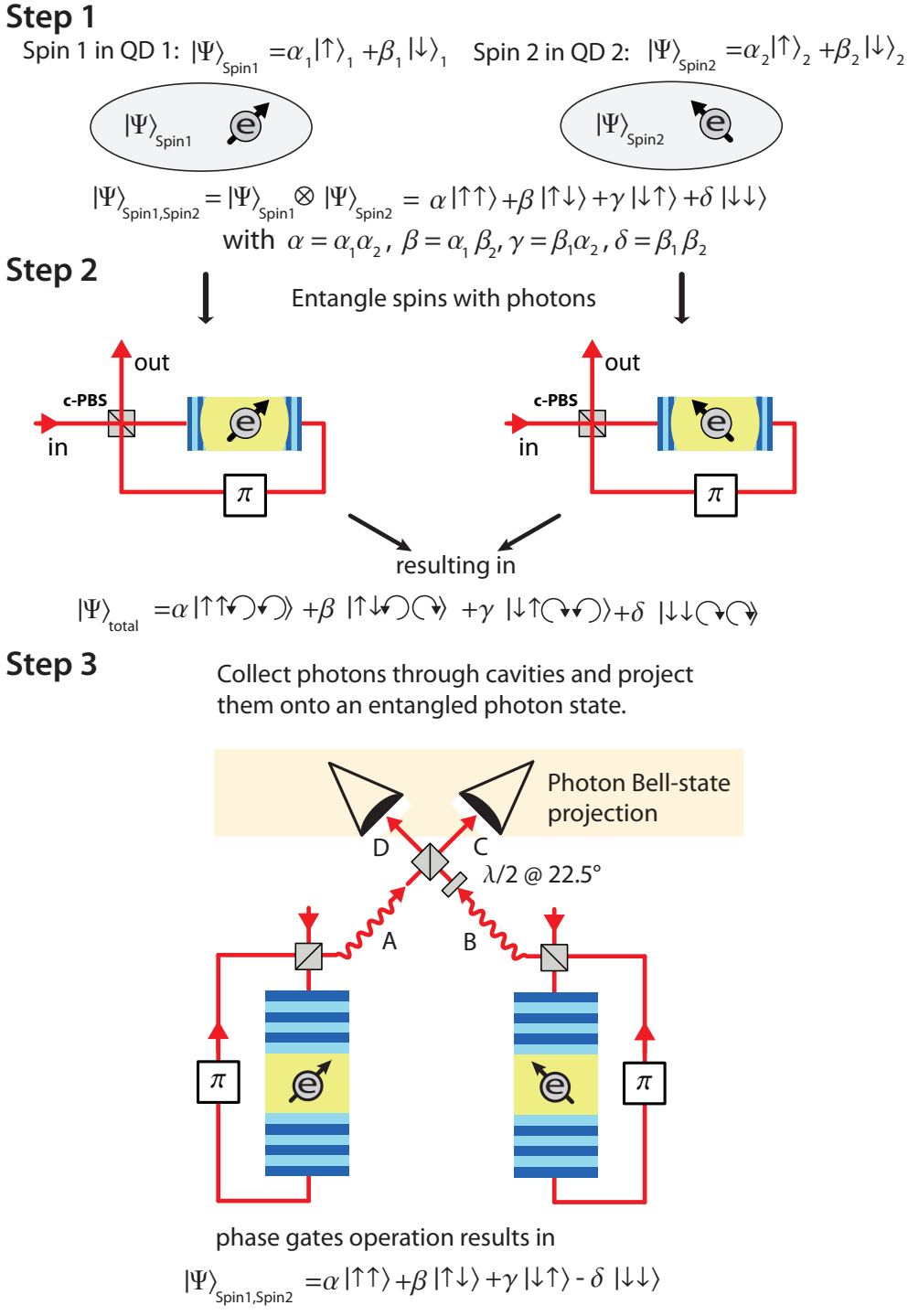

Figure 1.1: *Outline of scheme for a two-qubit phase gate.*

2. Each electron spin will be entangled with a photon using cavity QED being described by a total wave function $|\Psi\rangle_{total} = |\Psi\rangle_{Spin1,photon1,Spin2,photon2}$:

$$\begin{aligned} |\Psi\rangle_{total} &= \alpha\,|\uparrow\rangle_1\,|\uparrow\rangle_2\,|\circlearrowleft\rangle_A\,|\circlearrowleft\rangle_B + \beta\,|\uparrow\rangle_1\,|\downarrow\rangle_2\,|\circlearrowleft\rangle_A\,|\circlearrowright\rangle_B + \\ &\quad \gamma\,|\downarrow\rangle_1\,|\uparrow\rangle_2\,|\circlearrowright\rangle_A\,|\circlearrowleft\rangle_B + \delta\,|\downarrow\rangle_1\,|\downarrow\rangle_2\,|\circlearrowright\rangle_A\,|\circlearrowright\rangle_B\,. \end{aligned} \quad (1.4)$$

3. Through optical cavities, optical modes and linear optical elements the two photons will then be projected onto an entangled state:

$$\Psi_{C,D} = \frac{1}{2}\left\{|\circlearrowleft\rangle_C\,|\circlearrowleft\rangle_D + |\circlearrowleft\rangle_C\,|\circlearrowright\rangle_D + |\circlearrowright\rangle_C\,|\circlearrowleft\rangle_D - |\circlearrowright\rangle_C\,|\circlearrowright\rangle_D\right\}. \quad (1.5)$$

This will project the spin qubits onto a state that is equivalent to the action of a two-qubit gate [22, 23]:

$${}_{C,D}\langle\Psi \mid \Psi\rangle_{total} = |\Psi\rangle_{Spin1,Spin2} = \alpha\,|\uparrow\uparrow\rangle + \beta\,|\uparrow\downarrow\rangle + \gamma\,|\downarrow\uparrow\rangle - \delta\,|\downarrow\downarrow\rangle\,. \quad (1.6)$$

The fact that the $|\downarrow\rangle_1\,|\downarrow\rangle_2$ component of the state has required a $-$sign makes this the action of a universal 2-qubit entangling gate.

In order to make the two photon projection measurement onto the state (1.5) we make use of the general quantum optics effect that a 50/50 beamsplitter (BS) followed by a photon detection in each arm acts as a projection onto the $|\Psi^-\rangle$ 2-photon Bell state:

$$\left|\Psi^-\right\rangle = \frac{1}{\sqrt{2}}(|0\rangle_i\,|1\rangle_j - |1\rangle_i\,|0\rangle_j), \quad (1.7)$$

where i, j are the labels for the two modes in question and where $|0\rangle$, $|1\rangle$ indicate the two basis states in an arbitrary orthogonal polarization basis. The three other Bell states will have two photons together detected in either arm C or D. To see this we show that a BS is *transparent* for the $|\Psi^-\rangle$ state. By inserting a $\lambda/2$ @ 22.5° in arm B the $|0\rangle_B$ and $|1\rangle_B$ basis states will be rotated into $\frac{|0\rangle_B+|1\rangle_B}{\sqrt{2}}$ and $\frac{|0\rangle_B-|1\rangle_B}{\sqrt{2}}$. Therefore the $|\Psi^-\rangle$ Bell state projection becomes a projection onto $\frac{1}{2}\left\{|0\rangle_A\,|0\rangle_B + |0\rangle_A\,|1\rangle_B + |1\rangle_A\,|0\rangle_B - |1\rangle_A\,|1\rangle_B\right\}$, as required for our scheme. The action of the BS is given by

$$\begin{bmatrix} C \\ D \end{bmatrix} = \frac{1}{\sqrt{2}}\begin{bmatrix} 1 & i \\ i & 1 \end{bmatrix}\begin{bmatrix} A \\ B \end{bmatrix}, \quad (1.8)$$

where the i indicates that a reflected EM field obtains a $\frac{\pi}{2}$ phase shift relative to the transmitted EM field. In order to properly include the

bosonic properties of photons we describe the *in* and *output* state of the BS in terms of creation operators active on the vacuum $|0\rangle_{AB} \equiv |0_{A_0}, 0_{A_1}, 0_{B_0}, 0_{B_1}\rangle$. With

$$|\Psi\rangle_{in} = \left|\Psi^-\right\rangle_{AB} = \frac{1}{\sqrt{2}}\left\{a^\dagger_{A_0}a^\dagger_{B_1} - a^\dagger_{A_1}a^\dagger_{B_0}\right\}|0\rangle_{AB} \tag{1.9}$$

after the BS action we obtain

$$\begin{aligned}
&|\Psi\rangle_{out} = \\
&= \frac{1}{2\sqrt{2}}\left\{(a^\dagger_{C_0} + ia^\dagger_{D_0})(a^\dagger_{D_1} + ia^\dagger_{C_1}) - (a^\dagger_{C_1} + ia^\dagger_{D_1})(a^\dagger_{D_0} + ia^\dagger_{C_0})\right\}|0\rangle_{CD} \\
&= \frac{1}{\sqrt{2}}\left\{a^\dagger_{C_0}a^\dagger_{D_1} - a^\dagger_{C_1}a^\dagger_{D_0}\right\}|0\rangle_{CD} \\
&= \left|\Psi^-\right\rangle_{CD}.
\end{aligned} \tag{1.10}$$

In the same way it is shown that

$$\begin{aligned}
|\Psi^+\rangle_{AB} &= \tfrac{1}{\sqrt{2}}\{|0\rangle_A|1\rangle_B + |1\rangle_A|0\rangle_B\} \quad \text{and} \\
|\Phi^\pm\rangle_{AB} &= \tfrac{1}{\sqrt{2}}\{|0\rangle_A|0\rangle_B \pm |1\rangle_A|1\rangle_B\}
\end{aligned}$$

after the beamsplitter give

$$\begin{aligned}
&\tfrac{i}{\sqrt{2}}\left\{a^\dagger_{C_0}a^\dagger_{C_1} + a^\dagger_{D_0}a^\dagger_{D_1}\right\}|0\rangle_{CD} \quad \text{and} \\
&\tfrac{1}{2\sqrt{2}}\left\{i(a^\dagger_{C_0})^2 + i(a^\dagger_{D_0})^2 \pm \left\{i(a^\dagger_{C_1})^2 + i(a^\dagger_{D_1})^2\right\}\right\}|0\rangle_{CD}.
\end{aligned}$$

In those three cases there will always be 2 photons detected together either in arm C or D. This completes the proof that the 50/50 BS with two single photon detectors forms a $|\Psi^-\rangle$ Bell state projection.

In a sense, the gate on two separated electron spins is implemented by quantum teleportation (the photons are projected onto an entangled state and through their initial entanglement with the two electron spins those spins become entangled). In Ref. [23] it is shown that the scheme can be modified to still work under photon loss and incomplete Bell-state projection. If the scheme can be shown to work for two spins it is a matter of linear scaling of the optical network (only neighboring QD/micropillar structures have to perform two-qubit interactions in order to build a global cluster state) to scale up to more and more qubits.

1.1.2 Required developments

The scheme outlined in Fig. 1.1 is well suited for a solid-state approach because no direct interactions between electron spins are needed to perform gate operations. The individual electron-spin states first have to be entangled with single photon states. This can be done using a spin dependent interaction with a polarization degenerate optical cavity mode. The interaction involves the QD trion state which has the important feature that the recombination energy of the additional electron-hole pair (exciton) is independent of the spin of the emitted photon and therefore independent of the initial and remaining electron spin. Note that the recombination energies of (neutral) excitons (without the presence of an additional electron) form a doublet with a small energy splitting due to electron-hole spin exchange interaction. Such an exchange interaction implies that the emitted photon is linearly polarized along the crystal axes. The trion state has two electrons in the singlet state ($J = 0$) and therefore no electron-spin dependent interaction. As a result any arbitrary electron spin qubit can in principle become entangled with a photon polarization qubit despite broken symmetries in the QD. The scheme requires an efficient single-photon QD interaction with tuning of the cavities and QDs in order to entangle photons with electron spins and to make two systems indistinguishable in frequency as needed to perform a Bell state projection, step 3 in Fig. 1.1.

1.2 Challenges

For implementation of the hybrid scheme outlined above the following tasks have to be performed:

1. Deterministic single spin positioning at the center of optical micro resonators
2. Control emitter-cavity interaction in the weak-coupling regime
3. Control emitter-cavity interaction in a polarization degenerate way
4. Single electron spin preparation in QDs
5. Entangle a single spin with a photon via the trion state
6. Enhance single spin coherence time
7. Couple multiple microcavity-QD systems
8. Entangle two electron qubits via the hybrid scheme

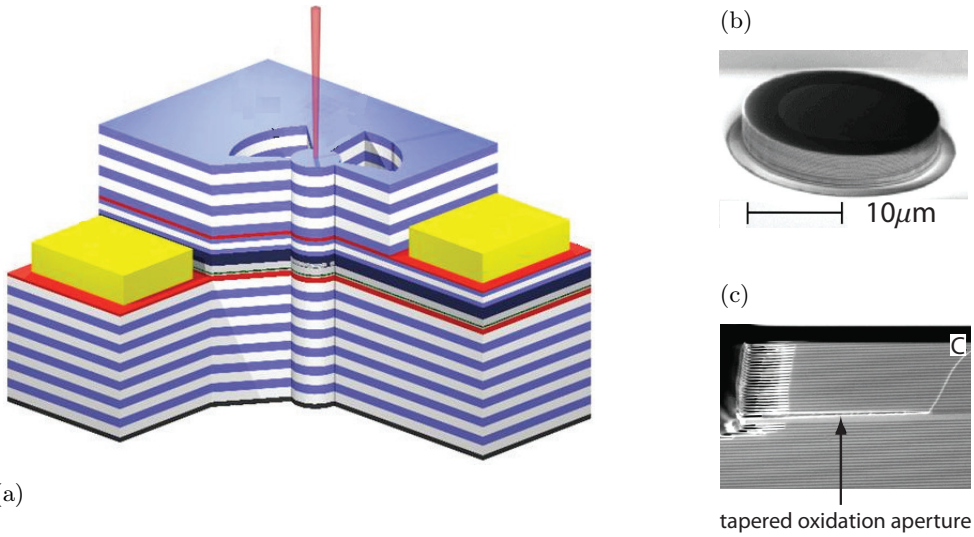

Figure 1.2: *(a) Schematic structure for the oxide apertured micropillars (for more details see Fig. 4.2). The active region with the embedded InGaAs/GaAs self-assembled QDs and the tapered oxide aperture are sandwiched between distributed Bragg reflection mirrors. Light is coupled normal to the sample surface (in the z-direction). (b) SEM image of a fully processed 22 μm diameter micropillar. (c) SEM cross-section image of an oxidized mesa calibration, showing the layer structure depicted in (a) including the tapered oxide aperture.*

As mentioned before, addressing those challenges requires a large research team with experts on material growth, sample fabrication, sample characterization, and quantum optical measurements. During my PhD research I have been partly involved in the sample fabrication but my main research concerns the optical study, control and fine-adjustment of the microcavity structures.

The **choice of materials** for the research presented in this thesis is In(Ga)As / $Al_xGa_{1-x}As$. The reason for using In(Ga)As / $Al_xGa_{1-x}As$, instead of other materials such as II-VI semiconductors, is that there is extensive knowledge on how to make high quality optical (in the range from 800 to 950nm) and electronic structures, especially at the University of California Santa Barbara (UCSB). Our research collaborators Prof. P.M. Petroff and Prof. L.A. Coldren (at the Materials and Engineering Departments at UCSB) have extensive experience and provide support in Molecular Beam Epitaxy (MBE) growth and optical studies of In(Ga)As /GaAs QDs and quantum

wells (III-V semiconductors). In particular Prof. Petroff first investigated self-assembled QDs at Bell Labs many years ago.

The **choice of cavity system** is the oxide-apertured micropillar structure shown in Fig. 1.2. The group of Prof. D. Bouwmeester has extensive experience with modeling, fabricating, and characterizing of both photonic crystal membranes and micropillars. Photonic crystal membranes are particular useful for integrated optics and for schemes to actively position QDs at the center of the optical mode and for frequency tuning. There is however one drawback and that is that it is very difficult to have polarization independent photon coupling to external field modes. It is possible to use efficient evanescence wave coupling through fibers near the surface of the photonic crystal however this approach is highly polarization dependent, which is detrimental for the above scheme. Another drawback is that the electronic control of the state of the QD is very challenging because of the thin membrane structure. Micropillars seem better candidates for the above scheme since they couple very efficiently to external optical modes, they can be made polarization degenerate, and doped layers can be integrated into the structures. A disadvantage of micropillar resonator, namely scattering from the sidewalls that limits the cavity quality to a few thousand, has been overcome by using a broad micropillar structure and confining the optical mode to a small inner region by inserting an oxidation aperture in the cavity (see Fig. 1.2). In this way we obtain cavity quality factors as high as 50.000 and 30% single photon collection efficiencies [24].

1.2.1 Deterministic spin positioning at the center of optical micro resonators

Figure 1.3(a) shows an optical imaging of an In(Ga)As QD in a layer of GaAs. The image is taken by scanning confocal microscopy with a computer controlled tracking system of the drift of the cryogenic sample mount (measurements have to be performed at 4K for good optical properties of the QDs). The position of the QD can be determined to within 10nm with respect to alignment marks (see Fig. 1.3(b)) pre-depositioned on the substrate.

1.2.2 Controlled emitter-cavity interaction in the weak-coupling regime

Once a single QD is positioned at the center of an optical mode of a micropillar it should also be matched in frequency with the mode. The common way to

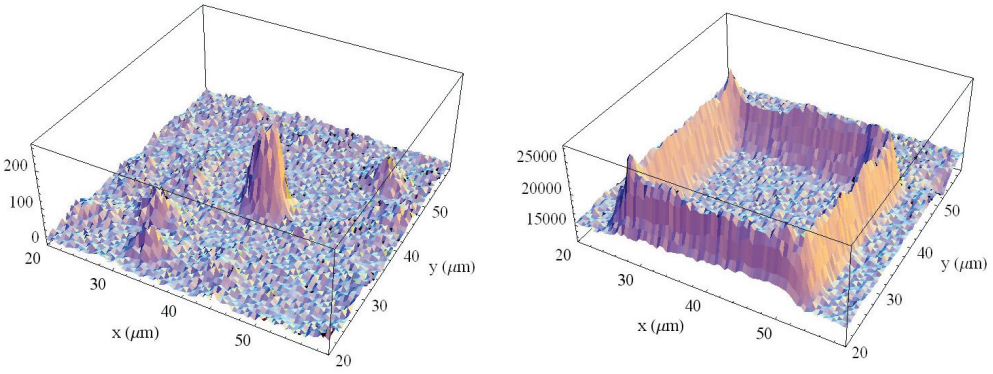

(a) (b)

Figure 1.3: *Optical images obtained by scanning optical confocal microscopy. (a) Emission from a single QD signal. By curve fitting the QD position can be determined to within* 10*nm. (b) Reflection signal from alignment markers.*

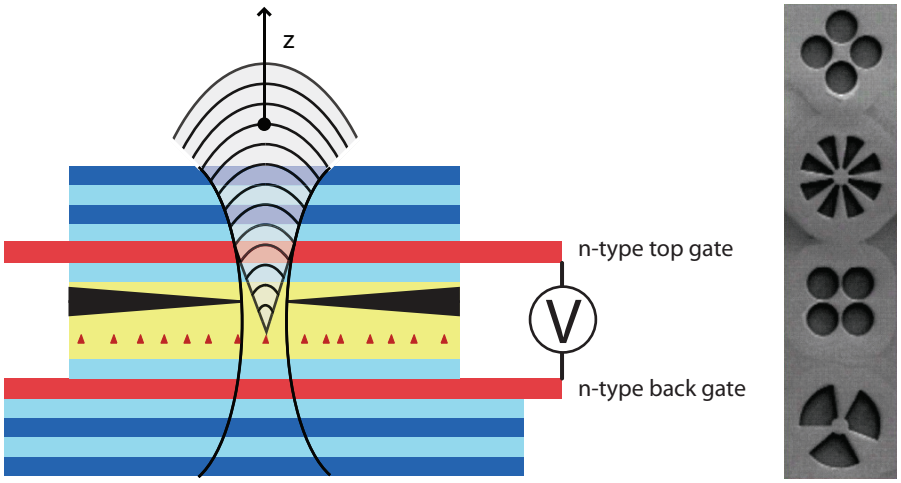

(a) (b)

Figure 1.4: *(a) Scheme for electrical contacting of n-doped Bragg layers leading to 'trench' designs (b) that allow implementation of oxidization micropillars with parallel contacting (courtesy of M.T.Rakher).*

achieve this is to use temperature tuning which will result in a relative shift between the frequencies of the QD emission and the optical mode. Temperature tuning is however undesirable because an increase in temperature will reduce the coherence time of the electron spins. As an alternative an applied electric field can be used to introduce a Stark shift of the transition frequency, typically of the order of a few meV. Applying an electric field means that doped layers have to be included close to the QDs embedded in the micropillar structure. A simple approach of providing a top and bottom gate will not work because the Bragg mirror 'shield' the QD. An extensive study showed that doped Bragg mirror layers close to the QDs, see sketch in Fig. 1.4(a), can provide the Stark tuning fields. To contact an individual Bragg layer on an individual etched micropillar is however unrealistic. Therefore the familiar pillar design is not adequate for this task. Since the optical mode is defined by a final oxidation step, holes (instead of pillars) can be etched in such a way that after the oxidation step there is still an optical mode defined via the oxidation taper. Figure 1.4(b) shows four 'trench' designs (top view on sample). The center of each figure is about 20μm in diameter and will after oxidation provide a 1 to 3μm diameter pillar mode; just like the familiar structures (Fig. 1.2). Given this design it is possible to electrically contact the desired Bragg layers at the side of the sample and control the voltage across an array of pillars, providing the desired frequency fine-tuning by a Stark shift.

Figure 1.5 shows the performance of such an electrical gating scheme on a Bragg structure with no pillars defined. The emission of a small number (3 to 6) of QDs has been monitored as function of the applied voltage between Bragg layers closely above and below the QDs. Discrete steps occur which indicate the charging of the QDs by additional electrons resulting in the exciton states X^0,X^{-1} and X^{-2}. Looking in the regions away from the discontinuities a small shift is observable which is the small Stark shift needed for the fine-tuning.

1.2.3 Controlled emitter-cavity interaction in a polarization degenerate way

As explained in Sect. 1.1 it will be crucial to have polarization degenerate interactions between a single QD and an optical resonator. Therefore the micropillar has to be degenerate in polarization. Usually there is a polarization splitting due to symmetry breaking by the optical axes of the materials and eventually due to fabrication imperfections. Some symmetry breaking is allowed since the optical resonator modes have a finite linewidth. As long as the symmetry breaking leads to shifts smaller than the linewidth the modes have significant overlap and are therefore largely degenerate. The oxidation-aperture pillar design can lead to large symmetry breaking due to different

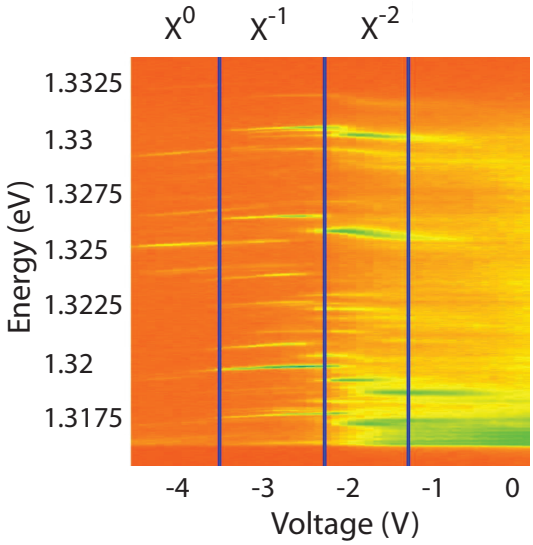

Figure 1.5: *Loading of QDs sandwiched between two Bragg layers of which the nearest layers are n-doped and electrically gated. The vertical lines mark discrete steps where the QDs get charged with additional electrons resulting in the exciton states X^0,X^{-1} and X^{-2} (courtesy of M.T.Rakher).*

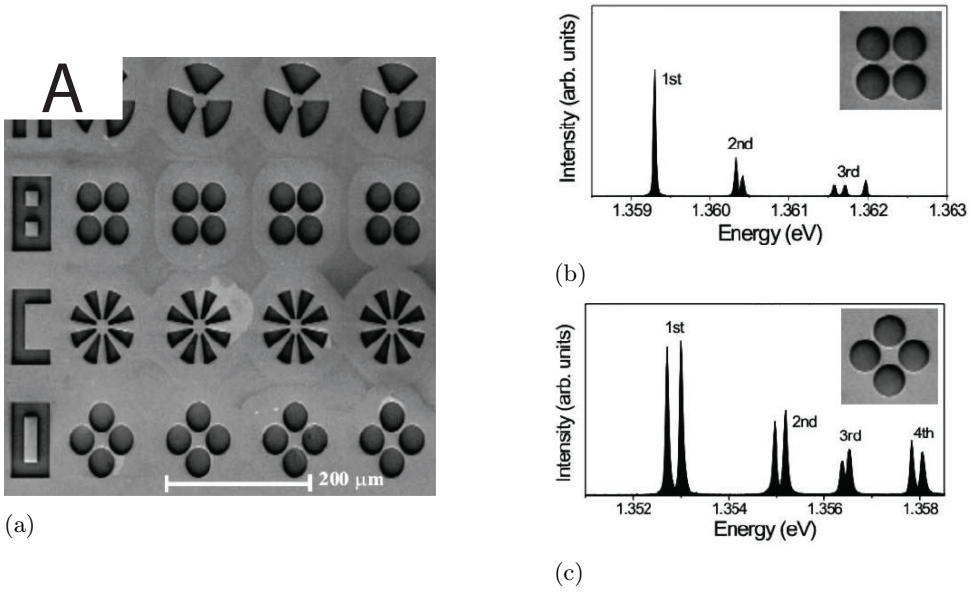

(a)

(b)

(c)

Figure 1.6: *(a) SEM image of arrays of different 'trench' pillars. (b) and (c) show experimental data for the different polarization splitting (especially for the first fundamental mode) of the same trench design but rotated by* 45 *degrees. Courtesy of M.T.Rakher.*

oxidation rates along the crystal axes. To investigate this effect, experiments have been performed in which the trench pillar design has been rotated by 45 degrees. Fig. 1.6 shows the remarkable difference between the polarization splitting in the two cases. This result shows that it should be feasible to optimize the geometry of the trenches (by rotations and possibly different hole sizes) such that after oxidization the fundamental pillar mode is close to degeneracy in polarization. To achieve the fine tuning of the birefringence we have investigated a technique to permanently alter strain in the sample via laser induced surface defects. The strain changes birefringence and as such can be used to tune the polarization degeneracy.

1.2.4 Single electron spin preparation in QDs

It is important to be able to load individual electrons onto a single QD (inside a polarization degenerate micropillar). This can be achieved by using the gated doped layer/Bragg mirror structure. But there is a complication in combining steps 2 and 4 namely that the Stark shift tuning range is very small $(1-3$ meV), because we can only apply a voltage up to the point that another

electron tunnels into the QD. The tunnel barrier has to be limited in order to preserve the possibility of loading the QD with a single electron. In short, the Stark tuning and the charging of the QD are to some extend complementary. Pillar fabrication and the frequency and spatial pre-positioning of the QDs have to be optimized to such a degree that post-fabrication tuning methods together with the small Stark shift as a fine-tuning method will be sufficient to prepare a single electron spin in a QD.

Loading the QD with a single electron is not sufficient for quantum information processing. A well defined initial quantum **state preparation** of the spin of the electron is required. This can in principal be achieved by optical pumping using resonant circular polarized light. Additional excitons in the QDs with the electron spin corresponding to the light polarization are created. The reemitted photons should have the same polarization as the pump and thereby forcing the additional stored electron spin to become orthogonal in spin to that of the optically pumped electrons [25]. Pauli Blockade interrupts the absorption and subsequent reemission of photons if a forbidden (spin -2, or 2) transition took place. Such 'dark' transitions occur as a result of heavy-light hole mixing. The absence of laser absorption is therefore also a signature of electron spin state preparation [9]. The lifetime of the spin state, directly related to the fidelity with which a specific state can be prepared, depends on the strength of electron spin flip (rotation) processes. Such processes can be strongly suppressed by introducing a Zeeman splitting, however this will remove the possibility of preparing an 'arbitrary' spin state [7]. The optical pumping technique requires the addition of magnetic fields and of narrow linewidth lasers.

1.2.5 Entangle a single spin with a photon via the trion state

Entanglement of an single electron spin state with a photon is necessary for implementation of the scheme. We utilize the trion state, that is the formation of an electron pair in the singlet state and an additional heavy hole, to map the spin state onto an optical state. Given the nature of the quantization axis for angular momentum of a QD (the QD confinement potential is much tighter in the z-growth direction than in the transversal direction due to the QD geometry), we can entangle a single electron spin state with a photon state by addressing the micropillar with resonant circularly-polarized light. The selection rules and a detailed description of this scheme is provided in Chap. 7 and published in [26]. In short, we can map an arbitrary electron spin state:

$$| \Psi_{el}\rangle = \alpha \, |\uparrow\rangle + \beta \, |\downarrow\rangle \tag{1.11}$$

onto an entangled electron-photon state

$$|\Psi\rangle = \alpha\,|\circlearrowleft^{\downarrow},\uparrow\rangle - \beta\,|\circlearrowright^{\uparrow},\downarrow\rangle, \tag{1.12}$$

by exciting with a right-circularly polarized photon $|\circlearrowright\rangle$ (oriented in direction of the z-axis). The superscript arrow of $|\circlearrowleft^{\downarrow}\rangle$ and $|\circlearrowright^{\uparrow}\rangle$ indicates the resulting propagation direction with respect to the z-axis. In case we measure a photon reflected by the cavity, we know that the electron spin is in the $|\uparrow\rangle$ state. And in case of a transmitted photon, the photon projects the electron spin onto the $|\downarrow\rangle$ state.

The principle of this operation is based on the Pauli exclusion principle which will prevent two electrons from having the same state. Therefore the absorption of say a spin 1 photon (producing a spin $-1/2$ electron and a spin $+3/2$ hole) will (not) be possible if the electron spin is $(-1/2)$ $1/2$. By placing the electron spin in a cavity that is modematched, in a polarization degenerate way, to the incoming photon mode the difference between whether or not the photon can be absorbed results in whether or not the photon is reflected or transmitted by the cavity. Here we make use of the fact that a balanced Fabry-Pérot optical cavity 100% transmit resonant light and that such a cavity with an absorber reflects the light.

This scheme is part of the mapping process that takes place in step 2 of Fig. 1.1. To investigate the entanglement between spin and photon it is important to have a near unity photon collection efficiency, otherwise the electron spin becomes entangled with the environment through the emitted photons absorbed by the environment. The use of micropillars is crucial in this respect.

1.2.6 Enhance single spin coherence time

Single quantum-dot single-spin relaxation time T1 of approximately 0.1ms has been measured at low temperatures [7, 9, 27, 28], and the single spin coherence time T2 has been measured to be approximately 10ns [10, 29–31]. For performing a single optical entangling operation between two spins those coherence properties are marginally sufficient. However, in order to perform many operations we have to investigate the origin of decoherence and develop ways of reducing decoherence. We keep in mind, that more challenging measurements using spin echo and nuclear polarization techniques have successfully been used to extend the coherence time to more than 1μs [10, 32].

Electron spin dephasing by phonon scattering in QDs is suppressed at temperatures below a few Kelvin, leaving interactions with nuclear spins as the dominant mechanism for electron spin dephasing [33]. The nuclear spins are

slowly changing, partly through their interaction with the electron, and therefore form an unknown spin environment, which causes an unknown electron spin precession. To some extend it is not appropriate to call this decoherence since in principal the dephasing can be undone by applying a π-pulse at half-time of the dynamical time interval of interest (assuming this interval is much shorter than the nuclear spin drift time) that will flip the electron spin state and therefore will reverse the dephasing in the second half of the dynamical interval. This spin echo technique has been well established in studies of nuclear magnetic resonances. To rotate a spin one typically has to apply a magnetic field, around which the spin will perform a precession. Such pulses can be obtained by using the magnetic field component of an optical field [34, 35]. It has been shown that dephasing can be suppressed by applying a train of light pulses synchronized to the phases of precessing spins [8].

1.2.7 Couple multiple microcavity-QD systems

In order to implement a two-spin qubit gate using intermediate trion and photon states two independent micropillars are needed, each with an electrically- and optically-controlled single QD, connected with each other through optical fibers and optical elements. Here the new micropillar design is again very advantageous since the pillars are mechanically as robust as a solid substrate (only holes are etched out of the solid-state sample and the actual pillars are defined by oxidation into the material). This allows the mechanical approach of antireflection-coated fiber tips right to the surface. Using a fiber core of typically 5μm in diameter pillar to fiber coupling efficiency of 80% should be possible.

1.2.8 Entangle two electron qubits via the hybrid scheme

The final step is the implementation of two-electron spin entanglement by teleportation measurements on corresponding photons. To achieve this we need two fiber-couple pillars tuned in resonance with each other and with the trion transitions and perform a Bell state projection measurement on the photons using fiber beam splitters and single photon detectors optimized around 940nm. To prove that the entangling gate operation works we would have to perform spin correlation measurements on spins again using the trion states.

In summary Sect. 1.2 listed the challenges to be addressed in order to implement the visionary scalable, hybrid approach (photon - solid state). This thesis mainly deals with the cavity aspects of this scheme. The following sections introduce the different theoretical frameworks that are fundamental

to the different aspects of this thesis in detail. For a profound introduction to this field see the book *Spins in Optically Active Quantum Dots Concepts and Methods* by Gywat, Krenner and Berezovsky [36].

1.3 Quantum dots

A QD is a nanoscale solid-state structure that confines electronic wavefunctions in all three spatial dimensions. This leads to discrete energy states for conduction band electrons and valence band holes. For this reason QDs are often referred to as *artificial atoms*. For our research it is of importance to work with *optically active* QDs, meaning the interaction between light and the charge carriers in the QD is sufficiently strong. Photons in the optical domain lead to electron transitions between the valence and the conduction band. The transitions can take place in two ways. In an optical absorption the electrons can be *driven* by a photon of sufficient energy from the valence to the conduction band. In the inverse process, luminescence, an electron relaxes from the conduction band to an unoccupied state in the valence band during which a photon is emitted.

1.3.1 Types of QDs

Three major types of QDs can be distinguished. These are colloidal QDs, lithographically patterned QDs and self-assembled QDs. The latter ones are introduced in detail as all experimental studies presented in this thesis are performed on self-assembled QDs. They have the advantage that they can be grown in layers and therefore allow integration in complex solid state structures that can for example contain contact layers for electrical control and Bragg mirrors.

1.3.2 Fabrication of self-assembled QDs

Self-assembled semiconductor QDs are grown by molecular beam epitaxy (MBE). Three different methods of growing self-assembled QDs are known: The Frank van der Merve, the Volmer-Weber and the Stanski-Krastanow method. The first two methods occur when the sum of the surface and interface energies is less or greater than the surface energy of the substrate. We use the Stanski-Krastanow method that takes place in strained systems such as In(Ga)As/GaAs, In(Ga)As/InP, SiGe/Si or CdSe/ZnSe. The strain is caused by the lattice mismatch of the substrate and the grown material.

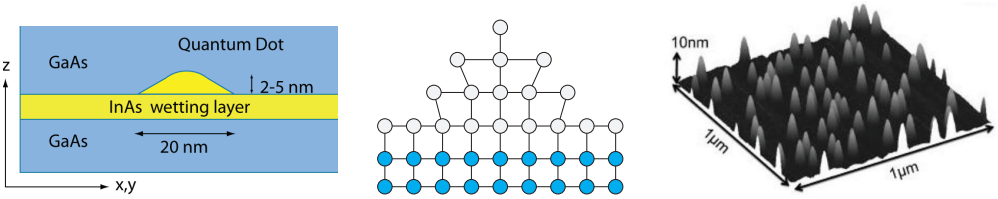

(a) (b) (c)

Figure 1.7: *(a) Scheme of QD island growth on substrate with approximate dimensions. (b) 7% lattice mismatch. (c) Atomic force micrograph of an ensemble of uncapped InAs islands on GaAs (courtesy of P.M. Petroff, T.A. Truong, and H.Kim, UC Santa Barbara).*

The QDs utilized in all samples in this thesis are self-assembled InAs QDs (during the growth Ga diffuses into the InAs leading to In(Ga)As QDs), with GaAs as a substrate and capping material. Figure 1.7(a) shows a schematic overview of the structure. In the very first step In and As atoms are deposited onto a GaAs substrate at high temperature. These atoms self-assemble defect-free and create atomic layers if the lattice mismatch of the substrate and deposits are small enough. The layer growth switches to the self-assembled island growth mode as the strain and the surface energy build up with continued deposition. Figure 1.7(b) illustrates the 7% lattice mismatch between the two materials. The total energy minimizes when building islands. See Fig. 1.7(c) for and AFM image of uncapped In(Ga)As islands on GaAs. Lateral dimensions of each island, meaning each QD, are usually $20-30$nm in diameter with a typical vertical height of $2-5$nm. Size and density of the QDs have an important effect on the optical emission characteristics; the tighter the confinement the larger the energy separation between levels and the more the optical properties shifted to shorter wavelength. A drawback of the Stanski-Krastanow method is the lack of control over positioning individual QDs. However, the MBE growth process allows to grow QDs with a different surface density on the same wafer. The density can vary from a few hundred dots per μm^2 to none. This fact enables to identify regions with a limited number of dots for further processing creating single QDs devices (see Chap. 5). As a last processing step, the uncapped QDs are overgrown with GaAs.

1.3.3 Optical and electrical properties

Exact size and composition, such as the concentration of In and As and the local strain in the structure, of a single QD are usually only roughly known. For that reason precise theoretical determination of the energy levels proves to be difficult, but models have been established that allow for a description of the optical and electrical properties that are consistent with experimental measurements.

Optical transitions

When an electron and a hole, particles of opposite charge, form a bound state, they are called an *exciton*. Excitons occur through Coulomb interaction in self-assembled InGaAs-QDs which constitute a few unique properties that make them excellent candidates for quantum information processing. Under weak optical excitation and low temperatures (< 30K) the QD exhibits a single narrow emission line (the single exciton recombination line X^0) with a linewidth as small as 5μeV [37]. Applying voltages across the QD can charge the QD with a single (or more) electron or hole. The resulting optical transitions will shift in energy due to electrostatic interactions. Strong optical excitation conditions give rise to more complicated recombination possibilities resulting in charged and multiple excitons that are energy separated from the single exciton line X^0. An advantage compared to atoms is the fact that QDs can optically be pumped non-resonantly above the bandgap of the GaAs; via a phonon relaxation process the QD will capture the optically excited charges. The typical peak emission wavelength of an InAs QD can be designed for the range of 0.9 to 1.2μm at 4K. Our samples typically emit around $930 - 955$nm.

Photoluminescence

The generation of electron-hole pairs in the material through optical excitation above the bandgap serves as an effective way to investigate the optical properties of a QD. The electron-hole pairs can relax into the QD and recombine radiatively (see Fig. 1.8). This measurement technique is called photoluminescence (PL) spectroscopy and provides information on the level structure of the QD. The optical excitation density controls the amount of carriers created and allows to relatively adjust the emission from different shells.

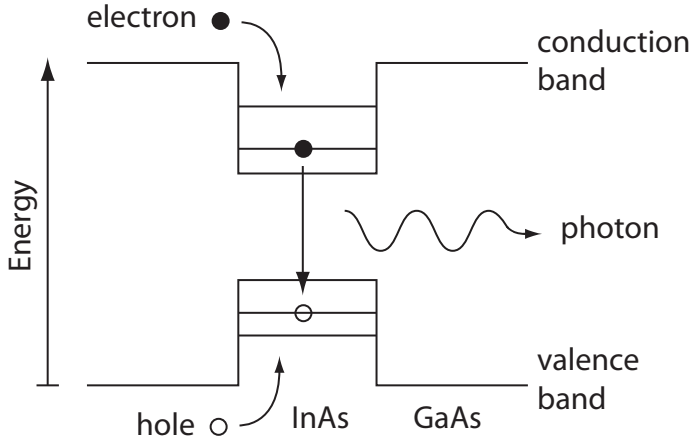

Figure 1.8: *Schematic recombination of an electron and a hole resulting in the emission of a photon. The InAs quantum is embedded in GaAs. When optically excited above the GaAs bandgap the electron-hole pairs relax into the QD where they can recombine.*

QD shell structure

In order to understand the characteristic QD transitions lines, which can be measured in PL spectroscopy, it is important to understand the energy levels in a QD. In its growth direction, the z-direction, a QD is rather small in dimension and its confinement can therefore be treated as a narrow quantum well. In the x-y-plane in comparison, the dimensions are larger (see Sect. 1.3.2) and the in-plane confinement can be approximated by a radially symmetric, two-dimensional harmonic potential. Thus, the effective bandgap energy $E_{g,eff}$ is the sum of the bulk bandgap energy E_g of the material and the energies of the electron E_z^e and the hole E_z^h as resulting from the strong confinement in the z-direction:

$$E_{g,eff} = E_g + E_z^e + E_z^h. \tag{1.13}$$

In the xy-direction the confinement is much weaker; the in-plane energies $E^a_{m_a,n_a}$ of electrons and holes are described by the two-dimensional harmonic oscillator energies with the quantum numbers m_a and n_a:

$$E^a_{m,n} = \hbar\omega_a(m + n + 1), \tag{1.14}$$

where $m, n = \{0, 1, 2, \ldots\}$. Finally, the total transition energy describing the electron-hole recombination is:

$$E_{transition} = E_g + \sum_{a=e,h} E_z^a + \sum_{a=e,h} E^a_{m_a,n_a} = E_{g,eff} + \sum_{a=e,h} E^a_{m_a,n_a}. \tag{1.15}$$

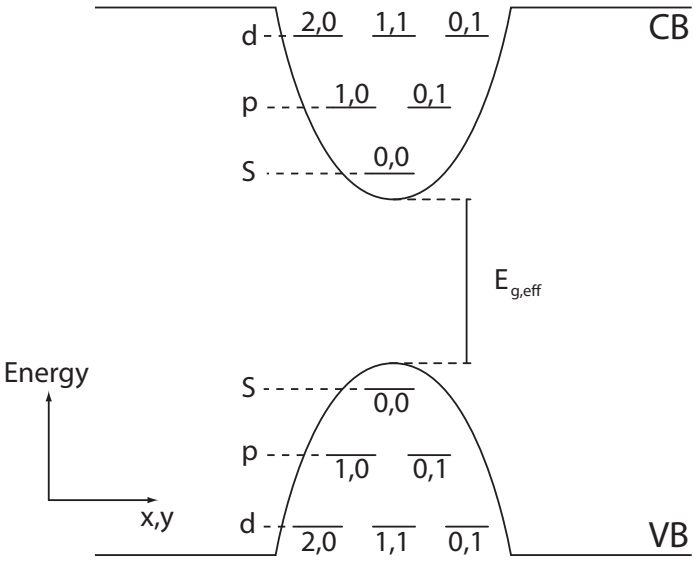

Figure 1.9: *QD energy levels with s,p,d shells for electrons and holes. The potential is harmonic resulting in an equal energy spacing between the levels.*

Following atomic physics, the quantum numbers n and m can be added and label the different shells. This first three shells, relevant for this thesis, are labeled s, p, d and correspond to $m+n=0$, $m+n=1$ and $m+n=2$. In the z-direction the orbital angular momentum is obtained by

$$L^a_{m,n} = \pm(m-n), \tag{1.16}$$

where the $+$ stands for electrons and the $-$ for holes. The degeneracy in energy of the i-th shell is given by $i+1$. This means that the s-shell has only one degenerate state ($\mid 0,0\rangle$) while the p-shell has two ($\mid 0,1\rangle$ and $\mid 1,0\rangle$) and the d-shell three states ($\mid 0,2\rangle$, $\mid 1,1\rangle$ and $\mid 2,0\rangle$). The QD energy levels for the first three levels for electrons and holes is schematically presented in Fig. 1.9. The Pauli Exclusion Principle determines the number of particles allowed in each orbital state. With a single-band approximation for the valence band, holes have a spin of $\pm\frac{3}{2}$. Electrons in the conduction band have a spin of $\pm\frac{1}{2}$. With two allowed spin states in each orbital level, the total degeneracy of the i-th shell is given by $2(n+1)$.

Dominant allowed optical interband transitions are between states with the same quantum number n and m. Additionally, the total spin M_z of the conduction band (S_z) and the valence band (J_z) must be ± 1. This results in creation of right (σ_+) or left (σ_-) oriented polarized photons. Therefore,

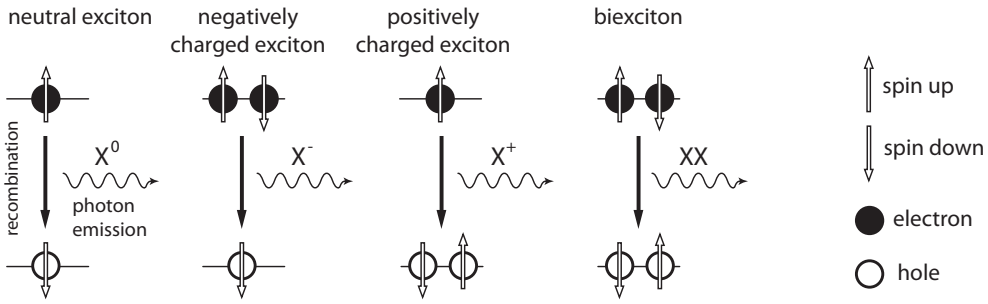

Figure 1.10: *QD charge state configurations for various electron hole states.*

recombination of electrons with spin $+\frac{1}{2}$ $(-\frac{1}{2})$ only takes place with holes of spin $-\frac{3}{2}$ $(+\frac{3}{2})$.

Important charged state configurations

For many quantum information proposals, and for this thesis, carrier configurations in the s-shell are of importance. Figure 1.10 illustrates the configurations for the four important exciton states in the s-shell. These are the X^0 (the neutral exciton line), X^- (the negatively charged single electron line), X^+ (the positively charged single hole exciton line) and XX (double exciton line or biexciton line) of a QD. For the first three states additional configurations with inverted spins exist resulting in inverted polarization of the emitted photon. The states described are optically active and called *bright states*. Optically inactive states, referred to as *dark states*, arise when an electron and a hole have an angular momentum difference of ± 2 that is impossible to be achieved with an electric dipole transition.
Figure 1.5 experimentally shows some of the states applying an electrical field over the QD.

Band structure

Self-assembled InGaAs-QDs are III-V semiconductors with the symmetry of zinc-blende lattices. Close to their Γ-point ($k = 0$) the extrema of the relevant bands are parabolic. Figure 1.11 schematically shows the conduction band, the heavy-hole (HH), the light-hole (LH) and the split-off valence bands. In Fig. 1.11(a) the HH and the LH state is energetically degenerate. E_g is the bandgap energy and Δ_{SO} the spin-orbit energy. Growth of different thin layered semiconductor materials lifts this degeneracy and results in an energy splitting Δ_{LH} between the light-hole and heavy-hole state, see Fig. 1.11(b).

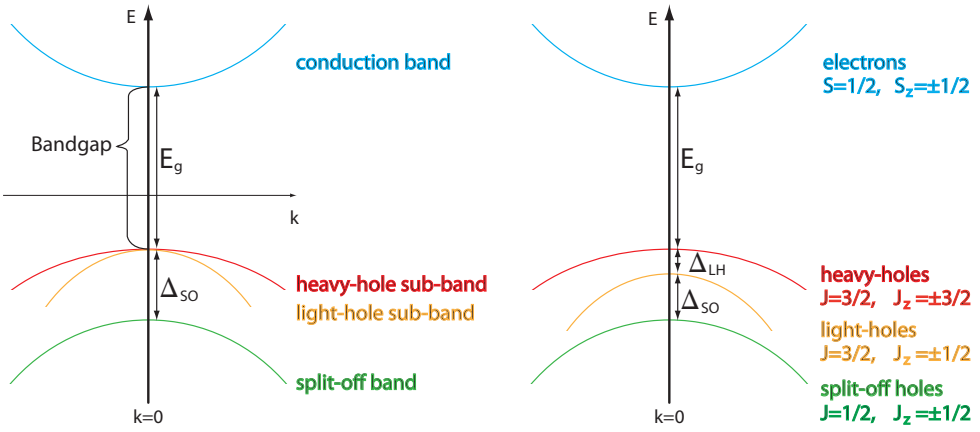

Figure 1.11: *Band structure of III-V semiconductors near the* Γ*-point for the energetically degenerate case (a) and with lifted degeneracy (b) resulting in a two-level system in the HH and LH sub-bands.*

This is the two-level system in the heavy-hole and light-hole bands important for hole-spin qubits.

Optical selection rules

Controlled electron spin and photon interaction can be implemented utilizing different transitions of spin-polarized electrons and holes in the QD. In the previous section Fig. 1.11(b) shows the optical transitions of the different bands. The energy of the exciting light can be chosen to only excite carriers from a specific band. Furthermore, using polarized light for excitation limits the possible transitions. Circularly polarized photons can only be absorbed if a change of the angular momentum of $\pm\hbar$ is possible, resulting in the possible optical transitions shown in Fig. 1.12. The focus of this thesis is the creation of electron-heavy hole pairs.

Electron-hole pairs can be created through resonant or non-resonant pumping. The latter method requires a doped layer near the QD as existing in our structures. When the excitation laser is tuned to the InGaAs wetting layer (temperature depended, around 865nm at 4K) a continuum of electron (spin up or spin down) states is added depending on the helicity of the excitation (σ_+ or σ_-). These electrons can relax into the QD and when the QD is singly doped, form a trion state consisting of two electrons and a hole. Using non-resonant pumping above the GaAs bandgap with arbitrary polarization is

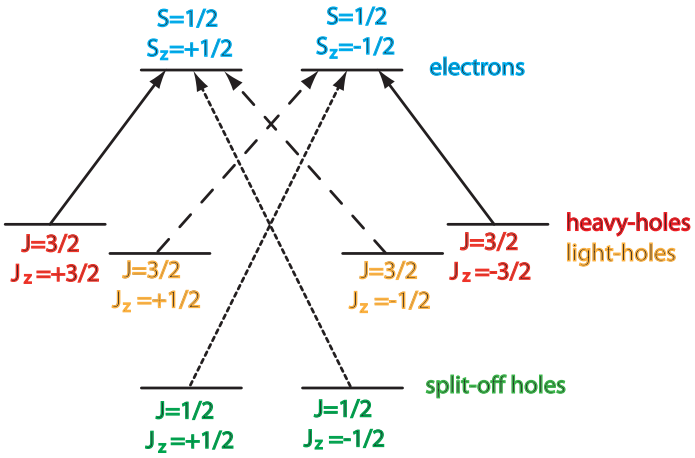

Figure 1.12: *Possible optical transitions exciting carriers with circularly polarized light. The solid arrows are the optical transition of interest: optical excitation of heavy holes.*

typically the first characterization method of our samples.
In the second method, we resonantly probe the QD with a narrow-linewidth laser. This technique is in particular important for chapters 6, 7 and 8. Fig. 1.13 summarizes the optical transitions. Shown are the two optically allowed transitions when exciting resonantly with circularly polarized light, that are photons with spin $s_z = +1$ (left side) or $s_z = -1$ (right side). The electron state with spin $S_z = +1/2$ ($|\uparrow\rangle$) excited with a photon with spin $s_z = +1$ leads to formation of a trion state. In that trion state two electrons form a singlet state that has a total spin of zero and therefore prevents electron-spin interactions with the hole spin $J_z = +3/2$ ($|\Uparrow\rangle$). The other configuration is achieved when an electron with spin $s_z = -1$ leads to a trion state where the hole spin is $J_z = -3/2$ ($|\Downarrow\rangle$). As mentioned before, it is important to note that the two dipole transitions are degenerate in energy which is a crucial requirement for achieving entanglement between photon spin and electron spin.

1.3.4 QD tuning via the Stark effect

When applying an external electric field to the QD, its transition frequencies shift.This effect is called the *quantum-confined Stark Effect* and allows for precise frequency tuning and therewith matching to cavity resonances. However, the absolute range for adapting the energy levels of the QD is rather small since additional charges will be captured by the QD if the applied field gets too large. The quantum-confined Stark effect is illustrated in Fig. 1.14. When

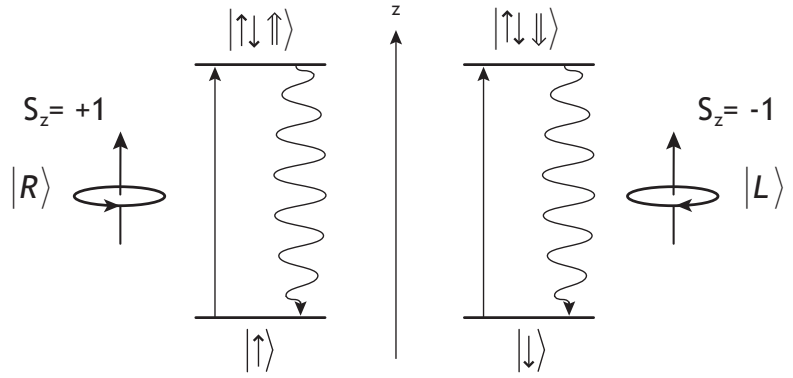

Figure 1.13: *Optical selection rules for the trion state.*

applying an electrical field to a QD (or as presented in the schematic to a quantum well) in the z-direction the wavefunctions experience a shift resulting in a reduction of the transition energy $\Delta E = E_C - E_V$. The quantum-confined Stark Effect additionally allows to control the number of particles in the QD and therefore address different states. Figure 1.5 shows a density plot of a QD spectra as a function of applied voltage. The differently charged states are visible and in addition to each state's wavelength tuning.

Implementation of controllable electric fields can be achieved by embedding the QDs in a diode structure. It is possible to load the QD either with electrons or holes. This is realized with a p-i diodes (holes) or n-i diodes (electrons). With p-i-n diodes both carriers can be injected and are used for our samples. Figure 1.15 schematically shows the the band structure of QD embedded in a such a p-i-n diode. When no bias voltage V_{app} is applied (Fig. 1.15(a)), the Fermi energy is designed to be lower than the conduction band energy and no current can flow. Once the structure is forward biased ($V_{app} > 0$), the electric field E_{app} drops over the intrinsic region. This lowers the energy of the p-type region in respect to the n-type region. Electrons move from the n-type region towards the p-type region while holes moves from the p-type region towards the n-type region resulting in an electric current. If they optically recombine in the QD in the intrinsic region emitted light can be observed. This phenomenon, the radiative recombination of electrons and holes, is called electroluminescence.

The electric field E_{app} is approximated by $E_{app} = V_{bi} - V_{app}/d_{instrinsic}$, where V_{bi} is the build-in potential difference and $d_{instrinsic}$ the length of the intrinsic region. V_{bi} depends on the doping of the n-type and p-type regions

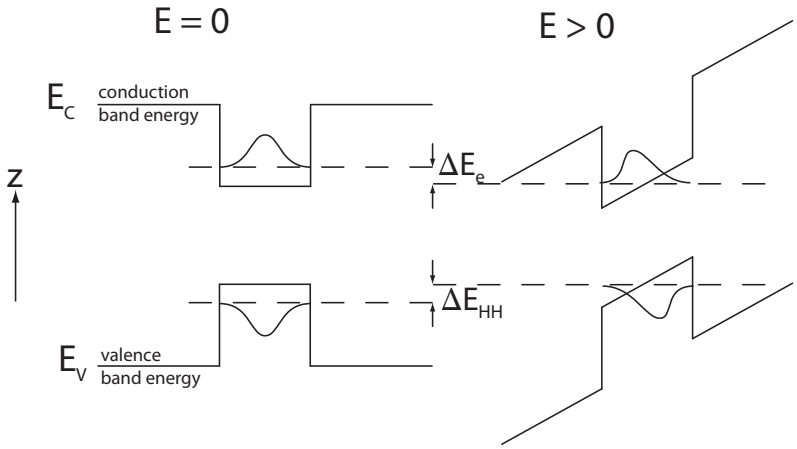

Figure 1.14: *Quantum-confined Stark effect. Left: No applied electrical field. Right: applied electrical field causing the electron states to shift to lower energies. The holes shift to higher energies*

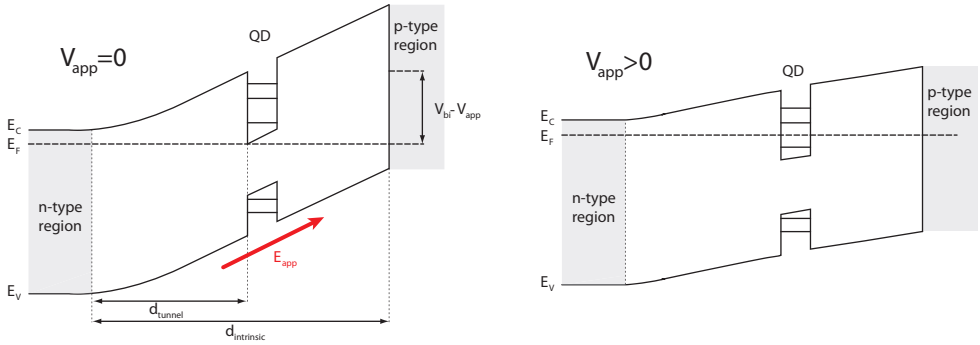

Figure 1.15: *Schematic band structure of a QD embedded in a p-i-n diode. (a) When no voltage bias is applied, the QD energy levels lie above the Fermi energy. When biasing the p-i-n structure, the static electric field across the intrinsic region E_{app} can be tuned so that electrons and holes can optically recombine in the QD.*

and is close to the bandgap of the material for high doping concentrations. Using GaAs for our samples, V_{bi} is around 1.5V, and $d_{instrinsic}$ typically around 500nm. Electric fields can be in the order of up to 300kV/cm.

1.4 Microcavities

In this section the effect of an optical resonator on the transition properties of QDs are described. Using MBE growth and nanofabrication techniques the QDs can be placed inside micron-size optical resonators. When the cavity is of the order of the emitters wavelength quantum mechanical effects on the cavity QD interaction can be observed that are absent for larger optical cavities.
The interaction between emitter and cavity by resonant recirculation is of interest for research with optical microcavities. Figure of merit for characterization of any optical microcavity is the the ratio of the quality factor Q and the mode volume V that is proportional to the Purcell factor. The Purcell factor describes the enhancement of the cavity optical mode density compared to free-space. In the field of cavity QED various types of microcavities are being investigated [38], for example micropillars; they exhibit a small cavity volume and relatively high Q [5], microtoroids; they can have an ultrahigh-Q [39] but have typically a fairly large mode volume, photonic crystal membrane cavities [40, 41]; they can have a very small mode volume V, microsphere whispering gallery resonators; extremely high Q but large V, and microdisks; high Q, fairly large V. Different microcavities are suited for particular novel devices or operation in certain coupling regimes. In this thesis we mainly investigate micropillar cavities and some results for photonic crystal cavities are presented in Sect. 5.3. Micropillar cavities consist of a high-refractive-index region sandwiched between two dielectric mirrors. The QDs are embedded in the center of the cavity between the mirrors such that they match the field maximum of the cavity and allow for highly-efficient polarization degenerate coupling to external cavity modes. We address single QDs electrically to have specific QD transitions interact with the cavity by implementing electrical gates. Light confinement is achieved by the combined action of distributed Bragg reflection (DBR) in the longitudinal direction along the post axis (the z-direction). In the lateral direction (in the x, y-plane) light confinement is usually provided by air-dielectric guiding. The fact that the light is coupled normal to the semiconductors sample surface allows for a high photon collection efficiency. As a disadvantage, micropillars do not allow for the smallest possible mode volume, because the cavity optical field extends into the Bragg mirror structure. Our cavities have Q factors that are currently limited to 50.000 [24]. However, Q factors up to 150.000 have been reported [42].

We work with modified micropillar structures that are not free-standing pillars but have remaining DBR mirrors surrounding the cavity region. Additionally, an oxide-aperture close to active layer with the QDs causes a difference in effective refractive index between the fully oxidized and the un-oxidized region. This provides an optical confinement effect in the x, y-plane [43,44]. The oxide-apertured micropillars relevant for this thesis are presented in detail in Sect. 3.2.

1.5 Cavity quantum electrodynamics

Cavity quantum electrodynamics (CQED) is the field of research that investigates the interaction between light confined in an optical cavity and atoms or QDs (artificial atoms). The spontaneous emission (SE) of an emitter coupled to a cavity is one important aspect of many experiments of interest. This section describes the essential theoretical concepts of CQED. First, we introduce the relevant cavity coupling parameters in order to describe a two-level dipole interacting with the quantized mode of an optical cavity using the Jaynes-Cummings model. By elaborating on the dynamics of the model we get a description for the weak and the strong coupling regime. Different approaches for deriving the full model exist in literature. I personally like the way of J.-M. Gérard as for instance published in [45]. But for reasons of completeness I follow C. Gerry and P. Knight in [46] while conceptually starting with [47].

1.5.1 Cavity coupling parameters

The key parameters to characterize a resonant dipole inside an optical cavity are the dipole-field coupling g, the photon cavity decay-rate κ, and the non-resonant dipole decay rate γ (see Fig. 1.16). Before discussing realistic conditions, consider the ideal case of a lossless microcavity. In this case the spontaneous emission becomes a reversible process that is described by Rabi oscillations. At Rabi frequency Ω a photon gets emitted and reabsorbed by the same 2-level system. The Rabi frequency depends on the initial number of photons in the cavity mode and even if this number is zero there can be a (vacuum) Rabi oscillation.

Experimentally, microcavities are never perfect and cavity losses have to be considered. The rate of these processes allows classification of two cases for the dipole-photon interaction:

- the strong coupling regime where $g > (\kappa - \gamma)/2$ and

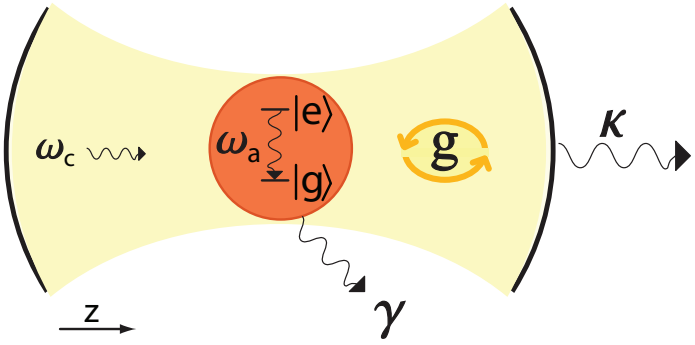

Figure 1.16: *Schematic of a probed cavity with a dipole inside. The key parameters to describe the cavity are the dipole-field coupling g, the photon cavity decay-rate κ, and the non-resonant dipole decay rate γ. The dipole can either be in the ground state $\mid g\rangle$ or the excited state $\mid e\rangle$.*

- the weak coupling regime where $g < (\kappa - \gamma)/2$

In literature, the different regimes of atom-light coupling are also often loosely defined by $g \gg (\kappa, \gamma)$ for the strong coupling regime and $g \ll (\kappa, \gamma)$ for the weak coupling regime [48–50]. For our cavity QED systems we typically are in the regime where $\gamma < g < \kappa$ which we classify as the weak coupling regime. When the rate of the loss /decoherence processes approaches the Rabi frequency, the dipole-photon interaction is still in the strong coupling regime. The system can then be regarded as damped. A photon emitted by the dipole is likely to be re-absorbed before it escapes the cavity. For an increased rate of the decoherence processes the system is over-damped, and photons emitted by the 2-level system will not be reabsorbed but leave the cavity instead. Eventually, the excited state of the dipole decays to the ground state.
This thesis mostly presents experiments exploiting the weak coupling regime. However, experimental observations of strong coupling are also presented in Chap. 5.2.

1.5.2 The Jaynes-Cummings model

Entanglement of states is fundamental to quantum information systems. An entangled state can be generated between an atom and an electromagnetic field. A well studied model to describe such an atom-field interaction for a two-level system is the Jaynes-Cummings model (JCM) [51]. It treats the atom, which in our case is the QD, as an electric-dipole interacting with a

quantized electromagnetic field. Its Hamiltonian looks as follows:

$$H = H_{field} + H_{atom} + H_{int} = H_0 + H_{int} \tag{1.17}$$

where H_{field} and H_{atom} express the light-field Hamiltonian and the atom Hamiltonian summarized as the free Hamiltonian H_0. The interaction part between the light and the atom is described by H_{int}. The electric dipole can be in two states, either in the ground state $|g\rangle$ or in the excited state $|e\rangle$, see Fig. 1.16. We define two bosonic operators: the annihilation operator a that lowers the cavity field and the creation operator $a^\dagger$ that raises it. Commutation relation $[a, a^\dagger] = 1$ applies to these operators.

For a cavity with mode frequency ω_c we can then write the free-field Hamiltonian as:

$$H_{field} = \hbar\omega_c \left(a^\dagger a + \frac{1}{2} \right). \tag{1.18}$$

As we are mainly interested in the dynamics of the system, we can neglect the zero-point energy term and the free-field Hamiltonian becomes:

$$H_{field} = \hbar\omega_c a^\dagger a \tag{1.19}$$

In order to describe the atom coupling, it is convenient to introduce the atomic transition operators

$$\sigma_+ = |e\rangle \langle g| \tag{1.20}$$

as the raising operator and

$$\sigma_- = |g\rangle \langle e| = \sigma_+^\dagger \tag{1.21}$$

as the lowering operator. Additionally, we define a population operator

$$\sigma_z = |e\rangle \langle e| - |g\rangle \langle g| . \tag{1.22}$$

σ_+, σ_- and σ_z are spin-$\frac{1}{2}$ Pauli operators which in atomic Hilbert space are expressed as 2×2 matrices:

$$\sigma_+ = \begin{bmatrix} 0 & 1 \\ 0 & 0 \end{bmatrix}, \qquad \sigma_- = \begin{bmatrix} 0 & 0 \\ 1 & 0 \end{bmatrix}, \qquad \sigma_z = \begin{bmatrix} 1 & 0 \\ 0 & -1 \end{bmatrix} \tag{1.23}$$

and obey commutation relations

$$[\sigma_+, \sigma_-] = \sigma_z, \qquad [\sigma_z, \sigma_+] = 2\sigma_+, \qquad [\sigma_z, \sigma_-] = 2\sigma_-. \tag{1.24}$$

The energy levels are $E_e = -E_g = \frac{1}{2}\hbar\omega_a$, where ω_a is the atomic frequency. Thus, with population operator σ_z we find the expression for the free atomic Hamiltonian:

$$H_{atom} = (E_e - E_g)\, \sigma_z = \frac{1}{2}\hbar\omega_a \sigma_z. \tag{1.25}$$

Interaction between the two-level atom and the cavity mode field can be described by the Schrödinger dipole interaction Hamiltonian

$$H_{int} = -\boldsymbol{d} \cdot \boldsymbol{E} \tag{1.26}$$

where $\boldsymbol{d}$ is the dipole moment matrix element between the excited $|e\rangle$ and the ground state $|g\rangle$. The cavity mode field $\boldsymbol{E}$ is of the form

$$\boldsymbol{E} = \boldsymbol{e}\left(\frac{\hbar\omega_c}{2\epsilon_M V}\right)^{\frac{1}{2}}(a + a^\dagger)\sin(kz) \tag{1.27}$$

where $\boldsymbol{e}$ is an arbitrary oriented polarization vector and ϵ_M the dielectric constant at maximum field intensity. The cavity mode volume V is defined as [52]

$$V = \frac{\iiint \epsilon(\boldsymbol{r})|E(\boldsymbol{r})|^2 d^3\boldsymbol{r}}{\epsilon_M |E(\boldsymbol{r}_M)|^2} \tag{1.28}$$

with $\boldsymbol{r}_M$ being the point of maximum field intensity.

The strength of the coupling can be expressed by a coupling parameter g. It describes the coupling of the transition dipole moment $\boldsymbol{d}$ to the electric field $\boldsymbol{E}$:

$$\hbar g = |\langle \boldsymbol{d} \cdot \boldsymbol{E} \rangle| . \tag{1.29}$$

We can now express the dipole interaction Hamiltonian (1.26) in terms of atomic transition operators

$$H_{int} = -d \cdot \left(\frac{\hbar\omega_c}{2\epsilon_M V}\right)^{\frac{1}{2}} \sin(kz)(\sigma_+ + \sigma_-)(a + a^\dagger). \tag{1.30}$$

If the atomic frequency ω_a and cavity frequency ω_c are close to resonance, rapidly oscillating terms can be neglected. These are the non-energy conserving and non-resonant terms $\sigma_+ a^\dagger$ and $\sigma_- a$ which are the creation of an exciton and photon and the annihilation of an exciton and a photon, respectively. This *rotating wave approximation* (RWA) leads to Hamiltonian H_{int} expressed by coupling constant g:

$$H_{int} = \hbar g(\boldsymbol{r})(\sigma_+ a + \sigma_- a^\dagger). \tag{1.31}$$

Looking at coupling constant g we can see that small mode volumes V enhance the microcavity performance: $g(\boldsymbol{r})$ is given by

$$g(\boldsymbol{r}) = \frac{\cos(\xi) g_0}{\hbar}\psi(\boldsymbol{r}) \tag{1.32}$$

with $\cos(\xi)$ being the polarization-dependent part, g_0 being the single-photon Rabi frequency and $\psi(\boldsymbol{r})$ the position-dependent part:

$$\cos(\xi) = \frac{\boldsymbol{d} \cdot \hat{e}}{d} \tag{1.33}$$

$$g_0 = \frac{d}{\hbar}\left(\frac{\hbar\omega_c}{2\epsilon_M V}\right) \tag{1.34}$$

$$\psi(\boldsymbol{r}) = \frac{E(\boldsymbol{r})}{|E(\boldsymbol{r}_M)|} \tag{1.35}$$

Finally, we have derived a complete expression for the Jaynes-Cummings Hamiltonian (in the RWA):

$$H_{JC} = \hbar\omega_c a^\dagger a + \frac{1}{2}\hbar\omega_a \sigma_z + \hbar g(\boldsymbol{r})(\sigma_+ a + \sigma_- a^\dagger). \tag{1.36}$$

The Jaynes-Cummings Hamiltonian does not include any coupling to an environment. These loss-mechanisms classified into the strong- and weak-coupling regime introduced in the previous section, are namely the spontaneous decay into the vacuum modes from the excited state $|e\rangle$ at rate γ and the decay of the field mode at rate κ. The following sections first introduce the dynamics of the JCM before elaborating on the theoretical description of the strong- and weak-coupling regime.

1.5.3 Dynamics of the Jaynes-Cummings model

Finding the stationary states of the JCM (1.36) yields a description for the transitions of the product states and their energy eigenstates caused by the interaction Hamiltonian H_{int}. For a cavity field with $|n\rangle$ photon states the interaction causes transitions of type

$$|e\rangle\,|n\rangle \leftrightarrow |g\rangle\,|n+1\rangle \tag{1.37}$$

or

$$|e\rangle\,|n-1\rangle \leftrightarrow |g\rangle\,|n\rangle\,. \tag{1.38}$$

These product states are referred to as the *bare states* of the JCM because they are the product states of the unperturbed atom and field. Given a fixed n, the dynamics are confined to the two-dimensional space (either (1.37) or (1.38)) and we can define the following product states:

$$|\psi_{1n}\rangle = |e\rangle\,|n\rangle \tag{1.39}$$

$$|\psi_{2n}\rangle = |g\rangle\,|n+1\rangle\,. \tag{1.40}$$

with their corresponding energy eigenstates are:

$$E_{1n} = \hbar\left(\frac{1}{2}\omega_a + n\omega_c\right) \tag{1.41}$$

$$E_{2n} = \hbar\left(-\frac{1}{2}\omega_a + (n+1)\omega_c\right). \tag{1.42}$$

The 2×2 subspace matrix representation of H follows from $H_{ij}^{(n)} = \langle\psi_{in} \mid H \mid \psi_{jn}\rangle$:

$$H = \begin{bmatrix} n\omega_c + \frac{1}{2}\omega_a & g\sqrt{n+1} \\ g\sqrt{n+1} & (n+1)\omega_c - \frac{1}{2}\omega_a \end{bmatrix} \tag{1.43}$$

When diagonalizing the matrix, the energy eigenvalues are as follows:

$$E_{\pm}(n) = \left(n+\frac{1}{2}\right)\hbar\omega_c \pm \frac{\hbar}{2}\sqrt{(\omega_a-\omega_c)^2 + 4g^2(n+1)}. \tag{1.44}$$

The second term corresponds to the Rabi frequency which includes the effects of the detuning $\Delta = \omega_a - \omega_c$:

$$\Omega(\Delta) = \sqrt{\Delta^2 + 4g^2(n+1)}. \tag{1.45}$$

The eigenstates $|n,\pm\rangle$ associated with the energy eigenvalues are called the *dressed states* and given by:

$$\mid n,+\rangle = \frac{1}{\sqrt{2}}\left(\frac{\Omega(\Delta)+\Delta}{\Omega(\Delta)}\right)^{1/2} \mid \psi_{1n}\rangle + \frac{1}{\sqrt{2}}\left(\frac{\Omega(\Delta)-\Delta}{\Omega(\Delta)}\right)^{1/2} \mid \psi_{2n}\rangle \tag{1.46}$$

$$\mid n,-\rangle = -\frac{1}{\sqrt{2}}\left(\frac{\Omega(\Delta)-\Delta}{\Omega(\Delta)}\right)^{1/2} \mid \psi_{1n}\rangle + \frac{1}{\sqrt{2}}\left(\frac{\Omega(\Delta)+\Delta}{\Omega(\Delta)}\right)^{1/2} \mid \psi_{2n}\rangle. \tag{1.47}$$

It is interesting to compare the energy splitting of the bare states and the dressed states which is $\hbar\Delta$ and $\hbar\Omega(\Delta)$ respectively. In case the dipole and the cavity are on resonance, the detuning Δ is zero. For this case, the bare states are degenerate in energy while a splitting for the dressed states remains. They states are related as follows:

$$\mid n,+\rangle = \frac{1}{\sqrt{2}}(\mid e\rangle \mid n\rangle + \mid g\rangle \mid n+1\rangle) \tag{1.48}$$

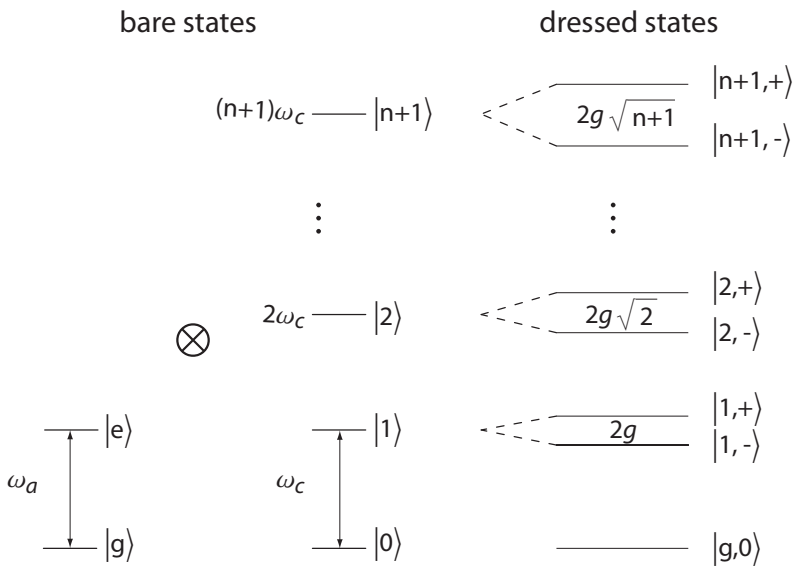

Figure 1.17: *Quantum level diagram with the uncoupled (right) and coupled levels (left). The uncoupled states are called bare states and the coupled eigenstates are referred to as dressed states.*

$$| n, - \rangle = \frac{1}{\sqrt{2}}(- | e\rangle | n\rangle + | g\rangle | n+1\rangle). \tag{1.49}$$

The different energy splittings are summarized in the quantum level diagram in Fig. 1.17.

For the non-ideal case, we have to include losses in our description for the dynamics of the JC model. For this purpose we include the photon cavity decay-rate κ and the non-resonant dipole decay rate γ that both describe the damping of the system. The approach is to see the damping being caused by interaction with a large reservoir of simple harmonic oscillators. In the Heisenberg picture the equation of motion for a general operator Θ becomes:

$$\frac{d\Theta}{dt} = -\frac{i}{\hbar}[\Theta, H] + \mathcal{L}(\Theta) \tag{1.50}$$

with $\mathcal{L}$ being the Markovian loss operator. Applying Eq. (1.50) to annihilation operator a and lowering operator σ_- yields:

$$\frac{da}{dt} = -i\omega_c a - ig\sigma_- - \kappa a \tag{1.51}$$

$$\frac{d\sigma_-}{dt} = -i\omega_a \sigma_- + ig\sigma_z a + \gamma\sigma_z\sigma_-. \tag{1.52}$$

The Hermitian conjugates of these correspond to creation operator $a^\dagger$ and raising operator σ_+. Assuming a very small photon number ($\langle n\rangle \ll 1$) the emitting dipole will almost always be in its ground state which is equal to $\langle\sigma_z\rangle \sim -1$. This allows us to replace σ_z with the expectation value -1. Additionally, when taking a vector oscillating at frequency ω with decay rate Γ, it adds a factor of $i\omega - \Gamma$ in the time derivation, so that Eqs. (1.51) and (1.52) can be written as:

$$\frac{dv}{dt} = \boldsymbol{M}v = (-i\omega - \Gamma)v \tag{1.53}$$

with

$$v = \begin{bmatrix} a \\ \sigma_- \end{bmatrix} \tag{1.54}$$

and

$$\boldsymbol{M} = \begin{bmatrix} -i\omega_c - \kappa & -ig \\ -ig & -i\omega_a - \gamma \end{bmatrix}. \tag{1.55}$$

Setting the eigenvalues of $\boldsymbol{M}$ equal to $-i\omega - \Gamma$ yields a description for the resonant frequency and the decay rate of the coupled system with losses:

$$\omega - i\Gamma = \frac{1}{2}(\omega_a + \omega_c) - \frac{i}{2}(\kappa + \gamma) \pm \sqrt{g^2 + \frac{1}{4}[(\omega_a - \omega_c) + i(\kappa - \gamma)]^2}. \quad (1.56)$$

This result compares to the ideal system with no losses ($\kappa = 0$ and $\gamma = 0$) expressed in Eqs. (1.44) and (1.45) when $n \sim 0$. The term under the square root in Eq. (1.56) indicates that Rabi oscillations can occur in case the term is real and not damped. A negative term implicates modification of the decay rate. Finally, we can see that the combination of the coupling constant g, the cavity and emitter decay rates κ and γ determines the regime the system is in.

1.5.4 The strong coupling regime

If $g > (\kappa - \gamma)/2$ the system is in the strong coupling regime. This is also the case if $\kappa \gg \gamma$ and therewith $g > \kappa/2$. This yields the square root in Eq. (1.56) to be positive. This regime is characterized by coherent energy transfer between the emitter and the dipole. The coupling between the emitter and the dipole dominates over the other decay channels. A characteristic signature for the strong coupling regime is the anticrossing of the cavity mode and the dipole emitter when tuned into resonance. Figure 1.18 shows the principal behavior for the anticrossing resulting from Eq. (1.56) as a function of the detuning $\Delta = \omega_a - \omega_c$. The solid lines show the coupled case and the dashed lines the uncoupled case. For the latter case the curves intersect at $\omega_a = \omega_c$. They act as asymptotes for the coupled-energy-lines, that do not intersect, for energies far from the resonant case at point $\omega_a = \omega_c$. The coupled states are referred to as *polaritons*. At the zero-detuning point the energy splitting between the two polariton states is at a minimum. This energy depends on the Rabi frequency, and therefore also on the coupling constant g:

$$\Delta E = 2\hbar\Omega = 2\hbar\sqrt{g^2 - \frac{1}{4}(\kappa - \gamma)^2}. \quad (1.57)$$

The energy splitting increases when g is maximized.

1.5.5 The weak coupling regime

In the weak coupling regime dissipative processes outweigh coherent coupling. The SE is irreversible and the QD emission relaxes towards its ground state. The regime is classified by $g < (\kappa - \gamma)/2$, corresponding to a negative term under the square root in Eq. (1.56). The emitter is still coupled to the cavity mode resulting in an enhancement of the spontaneous emission rate of the

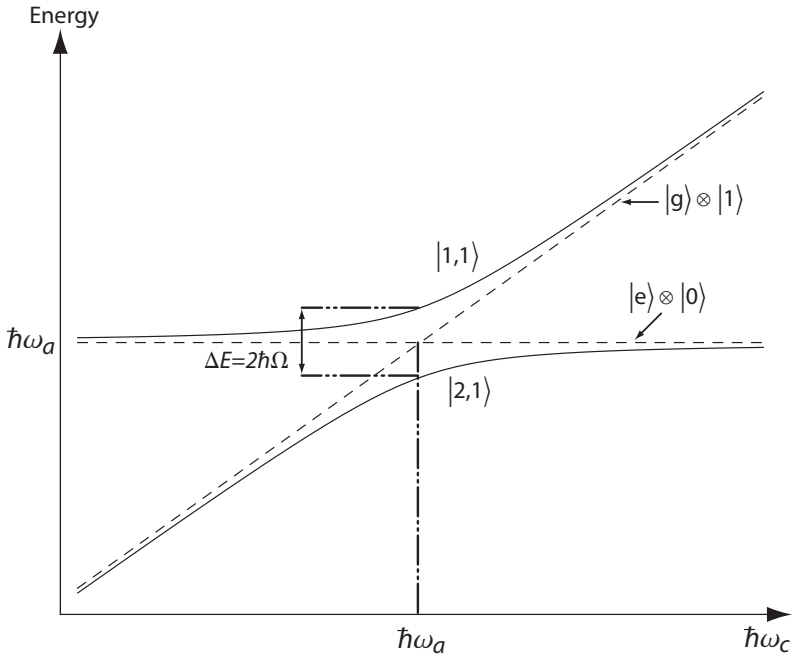

Figure 1.18: *Anticrossing of the coupled QD-cavity system calculated with the Jaynes-Cummings model. The energy of the polaritonic states (solid lines) and the uncoupled states (dashed lines) is plotted as a function of* $\Delta = \omega_a - \omega_c$.

emitter. We get an interesting relation when neglecting the non-resonant dipole decay rate γ (for our systems $\gamma << g, \kappa$) and only look at the relative effect of the photon cavity decay-rate κ and the dipole field coupling g. In case $\kappa \gg g$, linear expansion of the term under the square root in Eq. (1.56) leads to:

$$\omega_1 - i\Gamma_1 = \omega_a - i\frac{g^2}{\kappa} \tag{1.58}$$

$$\omega_2 - i\Gamma_2 = \omega_c - i\kappa + i\frac{g^2}{\kappa}, \tag{1.59}$$

where ω_1 and Γ_1 are the frequency and decay rate describing the dipole, and ω_2 and Γ_2 describing the cavity. A way of characterizing the enhancement of the spontaneous emission caused by the dipole-cavity coupling is provided in the next section. From Eq. (1.58) we see that dipole decay rate is g^2/κ, describing a cavity enhancement factor of $g^2/\kappa\gamma$.

1.5.6 Spontaneous emission and Purcell effect in microcavities

The spontaneous emission rate for a dipole resonantly coupled to a single-mode of a cavity in the weak-coupling regime is described by the Purcell effect. In 1946, Purcell predicted an enhancement of the spontaneous emission compared to free-space [53]. The so called Purcell factor describes this enhancement and conceptually is the same for any cavity. Different boundary conditions yield to different Purcell factors. The following derivation is given for the case that the emission frequency of the dipole couples exactly to the one and only existing single mode of the cavity of mode volume V_0.
Fermi's golden rule [53] describes the transition rate for spontaneous emission:

$$W = \frac{2\pi}{\hbar^2}|M_{12}|^2 g(\omega), \tag{1.60}$$

where M_{12} is the transition matrix element, and the density of states is described by $g(\omega)$. Because there is only one resonant mode such that

$$\int_0^\infty g(\omega) = 1, \tag{1.61}$$

the density of states $g(\omega)$ can be described by a Lorentzian function. Normalization fulfills Eq. (1.61). If we assume ω_a to be the frequency of the dipole transition and ω_c the resonance frequency of the cavity, the density of states writes as

$$g(\omega_a) = \frac{2}{\pi\Delta\omega_c} \cdot \frac{\Delta\omega_c^2}{4(\omega_a - \omega_c)^2 + \Delta\omega_c^2}, \tag{1.62}$$

where $\Delta\omega_c$ is the linewidth. For the resonant case ($\omega_a = \omega_c$) the formula reduces to

$$g(\omega_a) = \frac{2}{\pi\Delta\omega_c} = \frac{2Q}{\pi\omega_a}, \tag{1.63}$$

with Q being the quality factor defined by $Q = \frac{\omega}{\Delta\omega}$.
The matrix element for the electric dipole interaction in general writes as

$$M_{12} = \langle \boldsymbol{p} \cdot \boldsymbol{\varepsilon} \rangle. \tag{1.64}$$

or

$$M_{12}^2 = \xi^2 \mu_{12}^2 \varepsilon_{vac}^2, \tag{1.65}$$

where the factor ξ is the normalized dipole orientation factor given by:

$$\xi = \frac{|\boldsymbol{p} \cdot \boldsymbol{\varepsilon}|}{|\boldsymbol{p}||\boldsymbol{\varepsilon}|}. \tag{1.66}$$

For the **free-space** case we have to average over all possible orientations of the dipole with respect to the field direction. Therefore ξ^2 averages 1/3 because the dipole is randomly oriented in free-space

$$M_{12}^2 = \frac{1}{3}\mu_{12}^2 \varepsilon_{vac}^2. \tag{1.67}$$

However, for the case that the dipole moment is oriented parallel to the cavity mode E-field the electric dipole interaction becomes

$$M_{12}^2 = \xi^2 \mu_{12}^2 \varepsilon_{vac}^2 = \xi^2 \frac{\mu_{12}^2 \hbar\omega}{2\epsilon_0 V_0}. \tag{1.68}$$

Finally, we can express the transition rate for the spontaneous emission as given by Fermi's golden rule in Eq. (1.60) by substituting with Eqs. (1.68) and (1.62).

$$W_{cav} = \frac{2Q\mu_{12}^2}{\hbar\epsilon_0 V_0} \xi^2 \frac{\Delta\omega_c^2}{4(\omega_a - \omega_c)^2 + \Delta\omega_c^2}. \tag{1.69}$$

The **Purcell factor** F_P compares the free-space transition rate with the cavity transition rate for the spontaneous emission

$$F_P = \frac{W_{cav}}{W_{free}} = \frac{3Q}{4\pi^2 V_0} \left(\frac{\lambda}{n}\right)^3 \xi^2 \frac{\Delta\omega_c^2}{4(\omega_a - \omega_c)^2 + \Delta\omega_c^2}, \tag{1.70}$$

with $c/\omega = (\lambda/n)/2\pi$. λ is the free-space wavelength and n the refractive index of the active area of the cavity. At exact resonance ($\omega_a = \omega_c$) and with the dipoles oriented along the field direction the Purcell factor becomes

$$F_P = \frac{3Q}{4\pi^2 V_0} \left(\frac{\lambda}{n}\right)^3. \tag{1.71}$$

To summarize, the given Purcell factor in Eq. (1.71) is valid for the

1. resonant case of a dipole in a cavity,
2. with one single mode,
3. and the dipoles orientated along the field direction.

For the development of microcavities, the Purcell factor is an important figure of merit as it only depends on the cavity properties Q and V that can be modified by various design and fabrication techniques.

1.5.7 Cavity reflectivity with a single QD

Measuring the interaction between a cavity and a single QD in photoluminescence is one way of characterizing the solid-state QD-cavity QED system. Probing the system by reflectivity measurements is another way. A QD coupled to a cavity modifies its transmission and reflection spectra. In the ideal case a photon interacting on resonance with an electron spin in a cavity gets reflected. In other words, the cavity becomes reflective in case light is coupled to an absorber on resonance with the cavity. In the uncoupled case, that is, the QD transition is not resonant with the cavity, the cavity is transmissive. The cavity reflectivity is given by [54]:

$$R = \left| 1 - 2\kappa_1 \cdot \frac{\gamma - i(\omega - \omega_a)}{(\gamma - i(\omega - \omega_a)) \cdot (\kappa - i(\omega - \omega_c)) + g^2} \right|^2 , \tag{1.72}$$

where κ is the total cavity field loss rate and κ_1 the loss rate of the first mirror only. Equation (1.72) is illustrated schematically in Fig. 1.19 where we plot the reflectivity as a function of the frequency of the probed light for the coupled (solid blue curve) and the uncoupled ($g = 0$; dashed red curve) case for ($\kappa = \kappa_1$) In the ideal case, the height of the peak at the resonant frequency goes up to 1 in reflection.

An interesting aspect to be perceived from the reflectivity measurements is the dependence of the peak height on the probing beam intensity. Consider a few photons interacting with the cavity. The first photon that gets absorbed by the QD raises it to the excited state. As long as the QD remains in this excited state (described by the lifetime of the system), the cavity appears transmissive for further photons as there is no more state to be excited. Hence, at higher probing intensities a decreasing peak height can be observed. Literature describes this phenomenon as the *reflection peak nonlinearity* [54, 55]. Various aspects resulting from reflectivity measurements are investigated in Chap. 8.

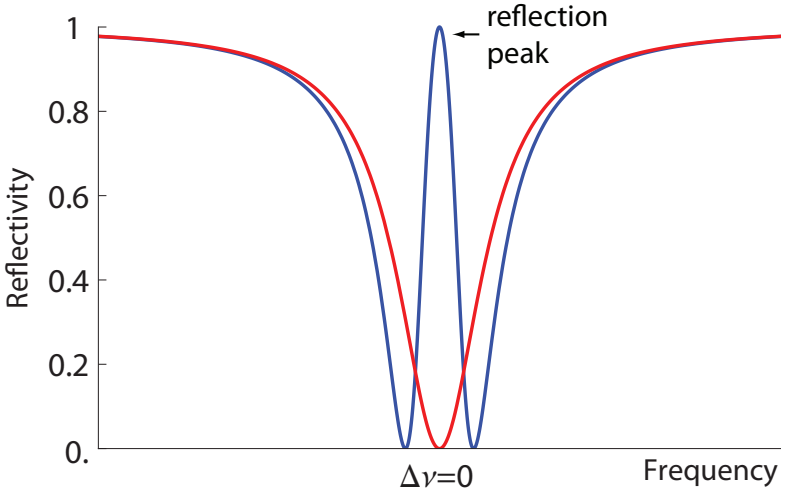

Figure 1.19: *Ideal reflection curves as a function of frequency for the coupled and uncoupled situation. If a QD transition is on resonance with the cavity, the cavity becomes reflective (blue curve) and at the resonance frequency all light is reflected, the peak in the dip goes to* 1*. If the QD is out of resonance, all light gets transmitted and a dip in the reflection can be observed at the cavity resonance (red curve).*